The Astrophysical Journal, 972:177 (13pp), 2024 September 10 https://doi.org/10.3847/1538-4357/ad5c64

SN 2024ggi in NGC 3621: Rising Ionization in a Nearby, Circumstellar-material-interacting Type II Supernova

W. V. Jacobson-Galán[1,21], K. W. Davis[2], C. D. Kilpatrick[3,4], L. Dessart[5], R. Margutti[1,6], R. Chornock[1], R. J. Foley[2], P. Arunachalam[2], K. Auchettl[2,7], C. R. Bom[8], R. Cartier[9], D. A. Coulter[10], G. Dimitriadis[11], D. Dickinson[12], M. R. Drout[13], A. T. Gagliano[14], C. Gall[15], B. Garretson[12], L. Izzo[15,16], D. O. Jones[17], N. LeBaron[1], H.-Y. Miao[18], D. Milisavljevic[12], Y.-C. Pan[18], A. Rest[10,19], C. Rojas-Bravo[2], A. Santos[8], H. Sears[3,4], B. M. Subrayan[12], K. Taggart[2], and S. Tinyanont[20]
[1] Department of Astronomy, University of California, Berkeley, CA 94720-3411, USA; wynnjg@berkeley.edu
[2] Department of Astronomy and Astrophysics, University of California, Santa Cruz, CA 95064, USA
[3] Center for Interdisciplinary Exploration and Research in Astrophysics (CIERA), Northwestern University, Evanston, IL 60202, USA
[4] Department of Physics and Astronomy, Northwestern University, Evanston, IL 60208, USA
[5] Institut d'Astrophysique de Paris, CNRS-Sorbonne Université, 98 bis boulevard Arago, F-75014 Paris, France
[6] Department of Physics, University of California, Berkeley, CA 94720, USA
[7] School of Physics, The University of Melbourne, VIC 3010, Australia
[8] Centro Brasileiro de Pesquisas Físicas, Rua Dr. Xavier Sigaud 150, 22290-180 Rio de Janeiro, RJ, Brazil
[9] Instituto de Estudios Astrofísicos, Facultad de Ingeniería y Ciencias, Universidad Diego Portales, Av. Ejército Libertador 441, Santiago, Chile
[10] Space Telescope Science Institute, Baltimore, MD 21218, USA
[11] School of Physics, Trinity College Dublin, The University of Dublin, Dublin 2, D02 PN40, Ireland
[12] Department of Physics and Astronomy, Purdue University, 525 Northwestern Avenue, West Lafayette, IN 47907, USA
[13] David A. Dunlap Department of Astronomy and Astrophysics, University of Toronto, 50 St. George Street, Toronto, Ontario M5S 3H4, Canada
[14] The NSF AI Institute for Artificial Intelligence and Fundamental Interactions, 77 Massachusetts Avenue, 26-555 Cambridge, MA 02139, USA
[15] DARK, Niels Bohr Institute, University of Copenhagen, Jagtvej 128, 2200 Copenhagen, Denmark
[16] Osservatorio Astronomico di Capodimonte, INAF, Salita Moiariello 16, Napoli, 80131, Italy
[17] Institute for Astronomy, University of Hawai'i, 640 N. A'ohoku Pl., Hilo, HI 96720, USA
[18] Graduate Institute of Astronomy, National Central University, 300 Zhongda Road, Zhongli, Taoyuan 32001, Taiwan
[19] Department of Physics and Astronomy, The Johns Hopkins University, Baltimore, MD 21218, USA
[20] National Astronomical Research Institute of Thailand, 260 Moo 4, Donkaew, Maerim, Chiang Mai 50180, Thailand
Received 2024 April 29; revised 2024 June 25; accepted 2024 June 25; published 2024 September 5

Abstract

We present UV–optical–near-infrared observations and modeling of supernova (SN) 2024ggi, a type II supernova (SN II) located in NGC 3621 at 7.2 Mpc. Early-time ("flash") spectroscopy of SN 2024ggi within +0.8 days of discovery shows emission lines of H I, He I, C III, and N III with a narrow core and broad, symmetric wings (i.e., "IIn-like") arising from the photoionized, optically thick, unshocked circumstellar material (CSM) that surrounded the progenitor star at shock breakout (SBO). By the next spectral epoch at +1.5 days, SN 2024ggi showed a rise in ionization as emission lines of He II, C IV, N IV/V, and O V became visible. This phenomenon is temporally consistent with a blueward shift in the UV–optical colors, both likely the result of SBO in an extended, dense CSM. The IIn-like features in SN 2024ggi persist on a timescale of $t_{\rm IIn} = 3.8 \pm 1.6$ days, at which time a reduction in CSM density allows the detection of Doppler-broadened features from the fastest SN material. SN 2024ggi has peak UV–optical absolute magnitudes of $M_{\rm w2} = -18.7$ mag and $M_{\rm g} = -18.1$ mag, respectively, that are consistent with the known population of CSM-interacting SNe II. Comparison of SN 2024ggi with a grid of radiation hydrodynamics and non–local thermodynamic equilibrium radiative-transfer simulations suggests a progenitor mass-loss rate of $\dot{M} = 10^{-2}\,M_{\odot}\,{\rm yr}^{-1}$ ($v_w = 50$ km s^{-1}), confined to a distance of $r < 5 \times 10^{14}$ cm. Assuming a wind velocity of $v_w = 50$ km s^{-1}, the progenitor star underwent an enhanced mass-loss episode in the last ∼3 yr before explosion.

Unified Astronomy Thesaurus concepts: Core-collapse supernovae (304); Type II supernovae (1731); Circumstellar matter (241); Radiative transfer (1335); Ultraviolet astronomy (1736)

1. Introduction

Shock breakout (SBO) from a red supergiant (RSG) star is characterized by an optical depth of $\tau \approx c/v_{\rm sh}$, where c is the speed of light and $v_{\rm sh}$ is the shock velocity. Consequently, the location and timescale of SBO photon escape is highly dependent on the density and extent of circumstellar material (CSM) that borders the RSG prior to explosion. In addition to light travel effects during SBO (Waxman & Katz 2017; Goldberg et al. 2022), the SBO signal can be significantly enhanced and elongated by the presence of high-density CSM directly above the stellar surface (Chevalier & Irwin 2011; Dessart et al. 2017; Haynie & Piro 2021). Once the shock has "broken out," the associated burst of high-energy radiation will "flash ionize" the surrounding medium—observationally this manifests as a hot supernova (SN) continuum riddled with recombination lines from ionized CSM. However, to overcome the recombination timescale of the flash ionized CSM ($t_{\rm rec} \propto 1/n_e \approx$ hours to days for $n \approx 10^{7-10}$ cm^{-3} and $\rho \approx 10^{-14}$–10^{-17} g cm^{-3} at $r < 2\ R_{\star}$, where $R_{\star}$ is the

[21] NSF Graduate Research Fellow.

progenitor radius), SN ejecta interaction with dense CSM provides continuous photoionization of the medium for sufficiently large CSM densities (e.g., $\rho \gtrsim 10^{-14}$ g cm^{-3}).

For Type II supernovae (SNe II) interacting with such dense CSM, high-energy photons will be emitted from the shock front as the postshock gas cools primarily through free–free emission ($T_{\rm sh} \approx 10^{5-8}$ K; Chevalier & Irwin 2012; Chevalier & Fransson 2017). This process then prolongs the formation of high-ionization recombination lines (e.g., He II, N III/IV/V, and C III/IV) present during the flash ionization phase. Intriguingly, as recombination line photons try to exit the CSM, they electron scatter off of free electrons in the ionized gas, which broadens the observed emission lines that will then appear as the combination of a narrow core and Lorentzian wings (i.e., "IIn-like features;" Chugai 2001; Dessart et al. 2009; Huang & Chevalier 2018). However, as the CSM density and optical depth to electron scattering drops, these electron-scattering profiles will fade on a characteristic timescale ($t_{\rm IIn}$), with the SN photosphere then revealing the fastest-moving SN material (Dessart et al. 2017; Dessart & Jacobson-Galán 2023; Jacobson-Galán et al. 2023, 2024).

Given the rapid evolution of CSM-interacting SNe II in their first hours to days, ultrarapid ("flash") spectroscopy is essential to both capture the SBO signal and persistent photoionization of dense CSM, and also to constrain the composition and mass-loss history of the progenitor star in its final year(s) before collapse (Gal-Yam et al. 2014; Khazov et al. 2016; Yaron et al. 2017; Terreran et al. 2022; Jacobson-Galán et al. 2023). To date, all-sky transient surveys have allowed for systematic discovery of SNe II within days of first light. Through modeling of early-time SN II spectra showing IIn-like features with non–local thermodynamic equilibrium (NLTE) radiative-transfer codes (e.g., CMFGEN; Hillier & Dessart 2012; Dessart et al. 2015), numerous single-object studies indicate enhanced RSG mass loss ($\dot{M} \approx 10^{-3}$–10^{-2} $M_\odot$ yr^{-1}, $v_w \approx 50$–100 km s^{-1}) in the final years before explosion (e.g., PTF11iqb, Smith et al. 2015; SN 2013fs, Dessart et al. 2017; Yaron et al. 2017; SN 2014G. Terreran et al. 2016; SN 2016bkv, Hosseinzadeh et al. 2018; Nakaoka et al. 2018; SN 2017ahn, Tartaglia et al. 2021; SN 2018zd, Zhang et al. 2020; Hiramatsu et al. 2021; SN 2019nyk, Dastidar et al. 2024; SN 2020pni, Terreran et al. 2022; SN 2020tlf, Jacobson-Galán et al. 2022; SN 2022jox, Andrews et al. 2024; SN 2023ixf, Bostroem et al. 2023; Jacobson-Galán et al. 2023; Smith et al. 2023; Teja et al. 2023; Zimmerman et al. 2024). Furthermore, sample studies suggest that >40% of SNe II discovered within 2 days of first light show IIn-like features from interaction with dense CSM (Bruch et al. 2021, 2023). Additionally, relative to standard SNe II, events with early-time IIn-like features, are incredibly bright in the UV (Irani et al. 2024; Jacobson-Galán et al. 2024).

In this paper we present, analyze, and model photometric and spectroscopic observations of SN 2024ggi, first discovered by the Asteroid Terrestrial-impact Last Alert System (ATLAS; Chen et al. 2024; Srivastav et al. 2024; Tonry et al. 2024) on 2024 April 11 (MJD 60411.14). SN 2024ggi was classified as an SN II (Hoogendam et al. 2024; Zhai et al. 2024) and is located at $\alpha = 11^{\rm h}18^{\rm m}22\overset{\rm s}{.}09$, $\delta = -32°50'15\overset{''}{.}26$ in host galaxy NGC 3621. We adopt a time of first light of MJD 60410.80 ± 0.34 days, which is based on the average between the times of last nondetection ($m_L = 19.5$ mag) and first detection $m_o = 18.9$ mag. To validate this estimate of first light, we first fit the ATLAS o-band light curve with a two-component power law with the REDBACK software package (Sarin et al. 2024) and derive a time of first light of MJD 60411.07 ± 0.01. Additionally, using a uniform prior distribution derived from the last ATLAS nondetection on MJD 60410.45, we fit the bolometric light curve of SN 2024ggi with a suite of hydrodynamical models (e.g., see Moriya et al. 2023; Subrayan et al. 2023), which constrains the time of first light to be MJD $60410.56^{+0.07}_{-0.12}$. Both methods yield consistent explosion epochs to that derived above from the phases of last nondetection and first detection. All phases reported in this paper are with respect to this adopted time of first light (δt). In this paper, we use a redshift-independent host-galaxy distance of 7.24 ± 0.20 Mpc (Saha et al. 2006) and adopt a redshift of $z = 0.002215$ based on Na I D absorption in high-resolution spectra of SN 2024ggi obtained with the NEID Spectrograph on the WIYN Telescope (private communication).

Given detection and classification during its infancy, SN 2024ggi represents an incredible opportunity to study the SBO phase of a CSM-interacting SN II in unprecedented detail. In Section 2 we describe the UV, optical, and near-infrared (NIR) observations of SN 2024ggi. In Section 3 we present analysis, comparisons, and modeling of SN 2024ggi's optical photometric and spectroscopic properties. In Section 4 we discuss the progenitor environment and mass-loss history prior to SN 2024ggi. Conclusions are drawn in Section 5. All uncertainties are quoted at the 68% confidence level unless otherwise stated.

2. Observations

2.1. Photometric Observations

The Ultraviolet Optical Telescope (UVOT; Roming et al. 2005) on board the Neil Gehrels Swift Observatory (Gehrels et al. 2004) started observing SN 2024ggi on 2024 April 11 ($\delta t = 0.79$ days). We performed aperture photometry with a 5″ region radius with uvotsource within HEAsoft v6.33 (NASA High Energy Astrophysics Science Archive Research Center (Heasarc), 2014),[22] following the standard guidelines from Brown et al. (2014).[23] In order to remove contamination from the host galaxy, we employed preexplosion images to subtract the measured count rate at the location of the SN from the count rates in the SN images and corrected for point-spread-function (PSF) losses following the prescriptions of Brown et al. (2014). We note that not all early-time UVOT observations are included in this analysis given the degree of saturation.

We obtained *ugri* imaging of SN 2024ggi with the Las Cumbres Observatory (LCO) 1 m telescopes from 2024 April 12 to April 26 (Program ANU2024A-004). After downloading the BANZAI-reduced images from the LCO data archive (McCully et al. 2018), we used photpipe (Rest et al. 2005) to perform DoPhot PSF photometry (Schechter et al. 1993). All photometry was calibrated using the Pan-STARRS 1 stellar catalog with additional transformations to Sloan Digital Sky Survey u band derived from Finkbeiner et al. (2016). For additional details on our reductions, see Kilpatrick et al. (2018). We also obtained photometry using a 0.7 m Thai Robotic Telescope at the Cerro Tololo Inter-American Observatory in the *ugriz* bands. Images are bias subtracted and field flattened. Absolute photometry is obtained using stars in the $10' \times 10'$

[22] We used the most recent calibration database (CALDB) version.
[23] https://github.com/gterreran/Swift_host_subtraction

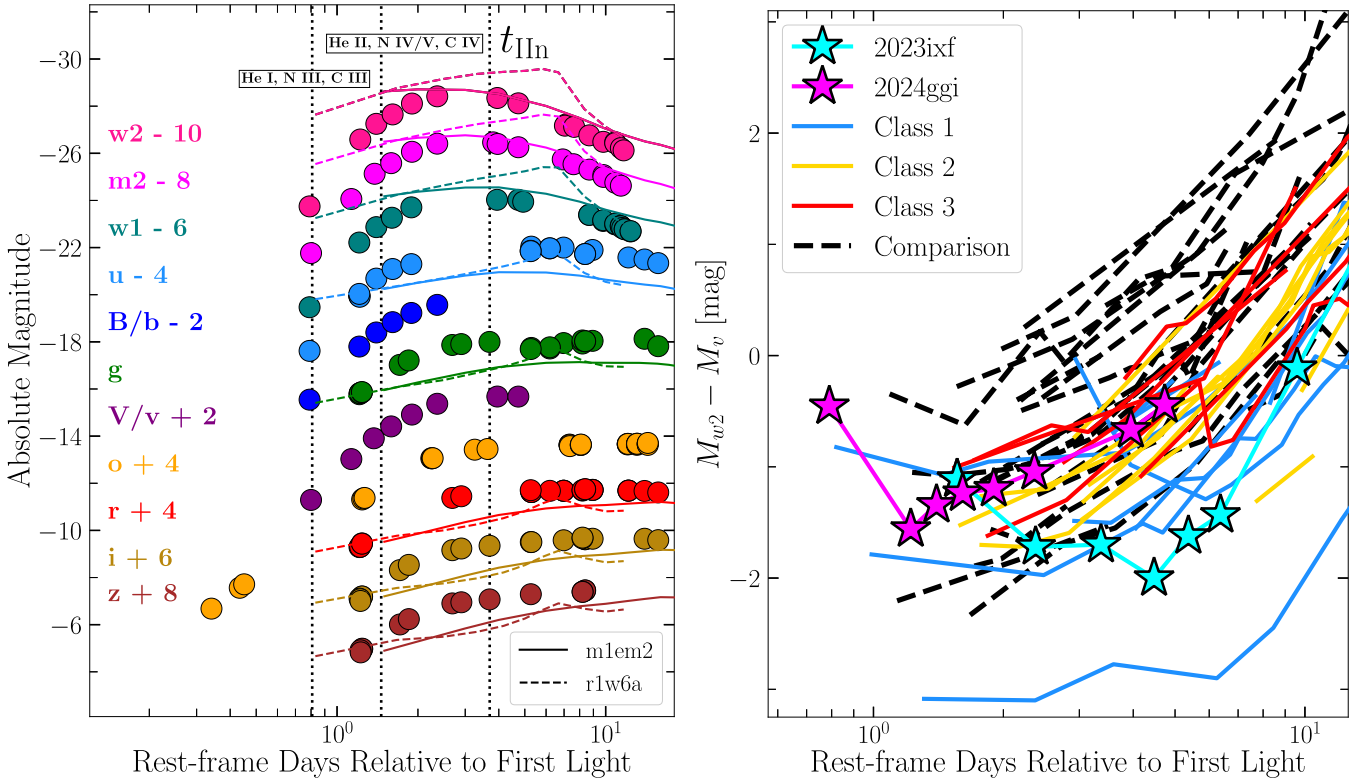

Figure 1. Left: multicolor light curve of SN 2024ggi (circles) with respect to time since first light (MJD 60410.80 ± 0.34) from the Swift, ATLAS, LCO, TRT, REM, T80s, and Lulin telescopes. Observed photometry is presented in the AB magnitude system and has been corrected for host-galaxy and Milky Way (MW) extinction. CMFGEN m1em2 and r1w6a model light curves are shown as solid and dashed lines, respectively. Right: early-time, reddening-corrected $W2 - V$ color plot for SN 2024ggi (magenta stars) and SN 2023ixf (cyan stars) with respect to gold- and silver-sample objects (red, yellow, and blue lines) and comparison-sample objects (black dashed lines; Jacobson-Galán et al. 2024). SN 2024ggi shows a blueward shift in color within the first ∼1 day since first light that is consistent with a rise in temperature and ionization (e.g., Figure 2).

field of view. We also observed SN 2024ggi with the Lulin 1 m telescope in the *griz* bands. Standard calibrations for bias and flat-fielding were performed on the images using IRAF, and we reduced the calibrated frames in photpipe using the same methods described above for the LCO images.

We also observed SN 2024ggi in the *grizH* bands with the Rapid Eye Mount (REM; Antonelli et al. 2003) telescope located in La Silla, Chile. REM is equipped with two cameras, which can observe simultaneously the same field of view ($10' \times 10'$) in the optical and NIR. Single images have been initially corrected for dark and flat frames observed each night. Then, images obtained with the same setup have been stacked and finally corrected for cosmic rays, all using a dedicated pipeline written in Python. Magnitudes were measured with aperture photometry, with a variable aperture size according to the seeing of the night, and calibrated against selected field stars from the Skymapper DR4 (Onken et al. 2024) that also have Two Micron All-Sky Survey *JHK*-band photometry. We also obtained *ugriz* imaging of SN 2024ggi with the 0.8 m T80S telescope at Cerro Tololo Inter-American Observatory, Chile. These were processed using the S-PLUS Transient Extension Program pipeline (Santos et al. 2024), including nonlinearity to recover detections of SN 2024ggi close to the saturation level. Additionally, we include *o*-band photometry by ATLAS that was downloaded from the forced photometry server (Tonry et al. 2018; Smith et al. 2020; Shingles et al. 2021). The complete multicolor light curve of SN 2024ggi is presented in Figure 1.

The MW *V*-band extinction and color excess along the SN line of sight is $A_V = 0.22$ mag and $E(B-V) = 0.07$ mag (Schlegel et al. 1998; Schlafly & Finkbeiner 2011), respectively, which we correct for using a standard Fitzpatrick (1999) reddening law ($R_V = 3.1$). In addition to the MW color excess, we estimate the contribution of galaxy extinction in the local SN environment. Using a high-resolution Kast spectrum of SN 2024ggi at $\delta t = 5.5$ days, we calculate Na I D2 and D1 equivalent widths (EWs) of 0.18 and 0.13 Å, respectively; these values are confirmed in a follow-up high-resolution Gemini spectrum at $\delta t = 9.2$ days. We use $A_V^{\rm host} = (0.78 \pm 0.15)$ mag × (EW$_{\rm NaID}$/Å) from Stritzinger et al. (2018) to convert these EWs to an intrinsic host-galaxy $E(B-V)$ and find a host-galaxy extinction of $E(B-V)_{\rm host} = 0.084 \pm 0.018$ mag, also corrected for using the Fitzpatrick (1999) reddening law.

2.2. Spectroscopic Observations

SN 2024ggi was observed with Shane/Kast (Miller & Stone 1993) and the Goodman spectrograph (Clemens et al. 2004) at the Southern Astrophysical Research (SOAR) telescope between $\delta t = 1.5$–9.3 days. For all of these spectroscopic observations, standard CCD processing and spectrum extraction were accomplished with IRAF.[24] The data were extracted using the optimal algorithm of Horne (1986). Low-order polynomial fits to calibration-lamp spectra were used to

[24] https://github.com/msiebert1/UCSC_spectral_pipeline

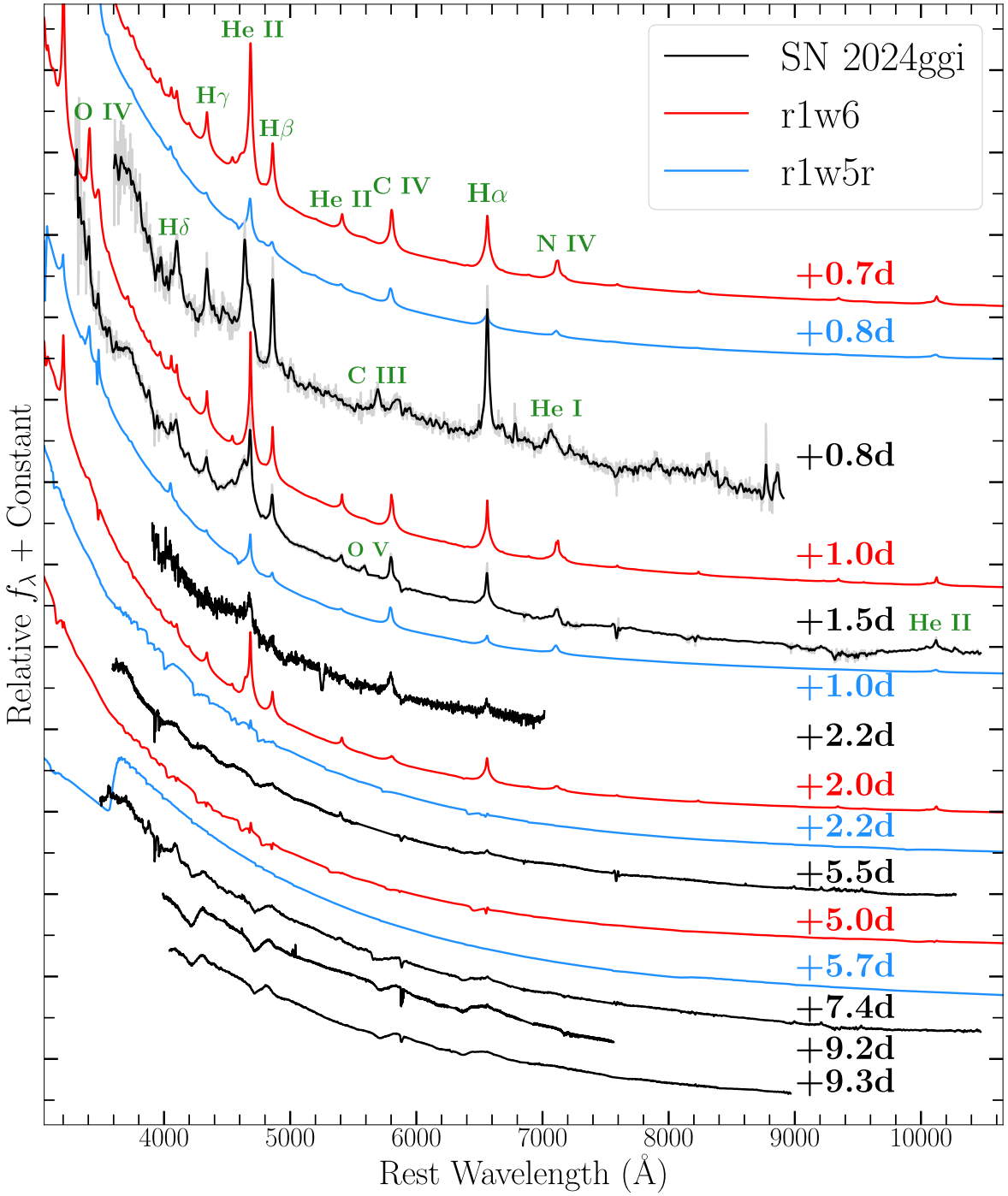

Figure 2. Early-time optical spectral series of SN 2024ggi (black) together with r1w6 (red) and r1w5r (blue) models from Dessart et al. (2017). The r1w6 and r1w5r models are characterized by wind mass-loss rates of $\dot{M} = (0.5\text{–}1) \times 10^{-2}\, M_\odot\ \mathrm{yr}^{-1}$ that extend to a CSM radius of $R_{\mathrm{CSM}} = (2\text{–}5) \times 10^{14}$ cm. The model spectra have been smoothed with a Gaussian kernel to match the spectral resolution of the data. Line identifications are shown in green. The appearance of He II, C IV, N IV/V, and O V after the $\delta t = +0.8$ day spectrum indicates a rise in ionization and temperature in SN 2024ggi as the breakout pulse and the subsequent continuous release of radiation from the shock diffuses through the CSM.

establish the wavelength scale and small adjustments derived from night-sky lines in the object frames were applied. SN 2024ggi spectra were also obtained with the Gemini Multi-Object Spectrograph (GMOS) at the Gemini-South Observatory at $\delta t = 9.2$ days and reduced with the Data Reduction for Astronomy from Gemini Observatory North and South (DRAGONS) pipeline (Labrie et al. 2023). Spectra were also obtained with the TripleSpec4.1 NIR Imaging Spectrograph (TSpec) at the SOAR telescope, and reduced using a modified version of `Spextool` (Cushing et al. 2004). Telluric corrections were applied using `xtellcor` presented in Vacca et al. (2003). Additional modifications to calibrations are described in Kirkpatrick et al. (2011).

In Figure 2 we present the complete series of optical spectroscopic observations of SN 2024ggi from $\delta t = 0.8$–9.3 days. In this plot, we also show the classification spectrum of SN 2024ggi at +0.8 days from the Lijiang 2.4 m telescope (Zhai et al. 2024), which we only use for narrow line

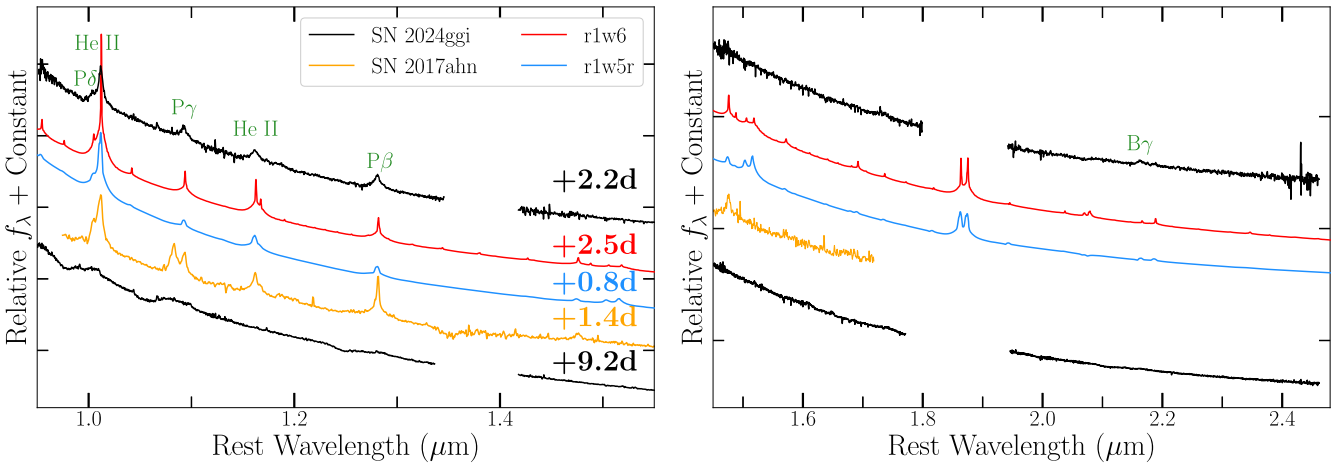

Figure 3. Left/right: NIR spectra of SN 2024ggi (black) and SN 2017ahn (orange) compared to the r1w5r (blue) and r1w6 (red) models from Dessart et al. (2017). Line identifications are shown in green.

Table 1
Main Parameters of SN 2024ggi

Host galaxy	NGC 3621
Redshift	0.002215
Distance	7.2 ± 0.2 Mpc[a]
Time of first light (MJD)	60410.80 ± 0.34
$E(B-V)_{\rm MW}$	0.07 mag[b]
$E(B-V)_{\rm host}$	0.084 ± 0.018 mag[c]
$M_{w2}^{\rm peak}[t_r]$	-18.7 ± 0.07 mag[3.0 ± 0.3 days]
$M_{m2}^{\rm peak}[t_r]$	-18.7 ± 0.07 mag[3.1 ± 0.3 days]
$M_{w1}^{\rm peak}[t_r]$	-18.4 ± 0.07 mag[3.2 ± 0.3 days]
$M_{u}^{\rm peak}[t_r]$	-18.2 ± 0.06 mag[3.5 ± 0.3 days]
$M_{g}^{\rm peak}[t_r]$	-18.1 ± 0.06 mag[6.5 ± 0.9 days]
$M_{r}^{\rm peak}[t_r]$	-17.8 ± 0.14 mag[8.6 ± 1.4 days]
$M_{i}^{\rm peak}[t_r]$	-17.7 ± 0.09 mag[8.5 ± 2.6 days]
$R_{\rm CSM}$	$\sim 5 \times 10^{14}$ cm
$M_{\rm CSM}$	(0.02–0.04) $M_\odot$
$\dot{M}$[d]	10^{-2} $M_\odot$ yr^{-1}
v_w	50 km s^{-1}
CSM composition	Solar metallicity[e]
Time of $\dot{M}$	$\sim$3 yr pre-SN

Notes.
[a] Saha et al. (2006).
[b] Schlegel et al. (1998) and Schlafly & Finkbeiner (2011).
[c] Stritzinger et al. (2018).
[d] Mass loss within $r < 10^{15}$ cm.
[e] Not varied in model grid.

identification. The complete optical–NIR spectral sequence is shown in Figures 2 and 3, and the log of spectroscopic observations is presented in Appendix Table A1.

3. Analysis

3.1. Photometric Properties

We present the complete early-time, multiband light curve of SN 2024ggi in Figure 1. Given the estimated time of first light, SN 2024ggi was first detected by ATLAS at $\delta t = 0.3$ days with an absolute magnitude of $M_o = -10.7$ mag and then quickly increased in luminosity to $M_o = -15.3$ mag by $\delta t = 1.2$ days. We fit high-order polynomials to the $w2$-, $m2$-, $w1$-, u-, g-, r-, and i-band light curves in order to estimate the peak luminosity and rise time of SN 2024ggi. All measurements are reported in Table 1, with the uncertainty in peak magnitude being the 1σ error from the fit and the uncertainty in the peak phase being found from adding the uncertainties in both the time of peak magnitude and the time of first light in quadrature. We find that SN 2024ggi has UV and optical peak absolute magnitudes of $M_{w2} = -18.7 \pm 0.07$ mag and $M_g = -18.1 \pm 0.06$ mag, respectively. Using the adopted time of first light, we estimate UV and optical rise times of $t_{w2} = 3.0 \pm 0.3$ days and $t_g = 6.5 \pm 0.9$ days, respectively.

In Figure 4, we compare the observed peak absolute magnitudes of SN 2024ggi to a sample of 74 SNe II from Jacobson-Galán et al. (2024). This sample includes 39 SNe II with detected IIn-like features in their early-time spectra: "gold-sample" objects have spectra at $\delta t < 2$ days and "silver-sample" objects only have spectra obtained at $\delta t > 2$ days. As discussed in Jacobson-Galán et al. (2024) and delineated by color in Figure 4, the gold- and silver-sample objects are classified in three main groups: "Class 1" (blue) show emission lines of N III, He II, and C IV (e.g., SNe 1998S, 2017ahn, 2018zd, 2020pni, 2020tlf, and 2023ixf); "Class 2" (yellow) have no N III emission but do show He II and C IV (e.g., SNe 2014G and 2022jox); and "Class 3" (red) only show weaker, narrow He II emission superimposed with a blueshifted, Doppler-broadened He II (e.g., SNe 2013fs and 2020xua). However, this classification scheme is epoch-dependent because the emission lines of O V/VI and N IV/V are also present in some objects such as SN 2013fs at $t < 1$ day owing to a more compact CSM than other CSM-interacting SNe II (Dessart et al. 2017; Yaron et al. 2017). Additionally, we present a comparison sample of 35 SNe II with spectra obtained at $\delta t < 2$ days but no detected IIn-like features.

As shown in Figure 4, SN 2024ggi is more luminous than most in the comparison sample SNe II without IIn-like features in all UV–optical filters. Furthermore, SN 2024ggi has a longer rise time in the UV filters than the comparison sample objects but comparable rise times in the optical filters. However, SN 2024ggi shows consistent UV–optical luminosities and rise times to gold- and silver-sample objects such as iPTF11iqb (Smith et al. 2015) and SN 2014G (Terreran et al. 2016). Additionally, SN 2024ggi has a comparable optical luminosity to SN 2023ixf but is less luminous in the UV by $\sim$0.7 mag. In the right panel of Figure 1, we also compare the early-time ($\delta t < 10$ days) $w2 - v$ color of SN 2024ggi to gold, silver, and comparison

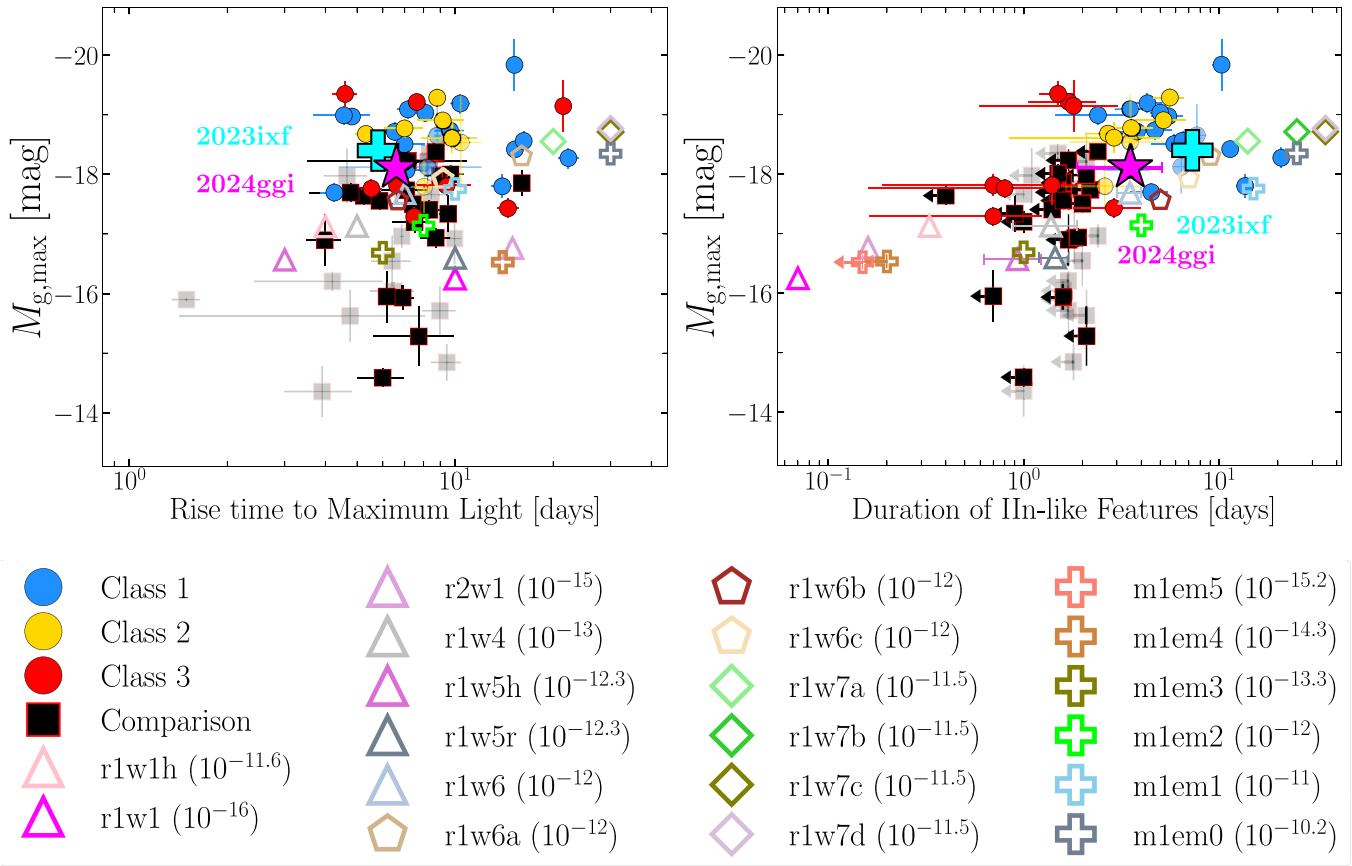

Figure 4. Peak g-band absolute magnitude vs. rise time (left) and duration of IIn-like features (right). Gold and silver samples are shown as blue, yellow, and red circles and the comparison sample is shown as black squares. Solid colored points represent the subsample of objects at $D > 40$ Mpc. Parameters from the CMFGEN model grid (Section 3.3) are plotted as colored stars, polygons, diamonds, and plus signs for CSM at 10^{14} cm (with density in units of g cm^{-3}) for each model displayed in parentheses. SNe 2024ggi and 2023ixf are shown as a magenta star and a cyan cross, respectively.

objects. Interestingly, SN 2024ggi shows a dramatic red-to-blue $w2-v$ color evolution of -0.46 mag to -1.56 mag between $\delta t = 0.8$–1.2 days, followed by consistently blue colors as it evolves redward in its first week. This unusual color evolution is also observed in other SNe II with IIn-like features such as SN 2023ixf (Hiramatsu et al. 2023; Hosseinzadeh et al. 2023; Li et al. 2024; Zimmerman et al. 2024), which was proposed as evidence for SBO in an extended dense CSM. This phenomenon is a product of the breakout pulse and the subsequent continuous release of radiation from the shock diffusing through the CSM (Dessart et al. 2017), and also corresponds to the phase during which the photosphere moves outward, initially at $R_\star$ and then out to the location of the electron-scattering photosphere ($R_{\tau=1}$; Dessart & Jacobson-Galán 2023). We also fit a blackbody model to the SN 2024ggi UV–optical spectral energy distribution and find blackbody temperature [radii] during this red-to-blue color evolution of $\sim$20 kK [5.3×10^{13} cm] at $\delta t = 0.8$ days and $\sim$23 kK [1.1×10^{14} cm] at $\delta t = 1.2$ days. Furthermore, we find that the blackbody temperature of SN 2024ggi peaks at $\sim$34 kK on $\delta t = 1.4$ days. This is a similar peak blackbody temperature to the 34.3 kK found for SN 2023ixf at $\delta t = 3.51$ days (Zimmerman et al. 2024). However, we note that these blackbody temperatures correspond to the temperature at the thermalization depth and that the blackbody radius is not equivalent to the location of the photosphere (i.e., $R_{BB} \ll R_{phot}$).

3.2. Spectroscopic Properties

We present our sample of optical observations for SN 2024ggi spanning from $\delta t = +0.8$ to $+9.3$ days in Figure 2. In the earliest spectrum at $\delta t = +0.8$ days, SN 2024ggi shows IIn-like features of H I ($\chi = 13.6$ eV), He I ($\chi = 24.6$ eV), N III ($\chi = 47.4$ eV), and C III ($\chi = 47.9$ eV). However, by the next spectral observation at $\delta t = +1.5$ days, SN 2024ggi shows prominent emission lines of He II ($\chi = 54.5$ eV), N III/IV/V ($\chi = 47.4/77.5/97.9$ eV), C IV ($\chi = 64.5$ eV), and O V ($\chi = 113.9$ eV), indicating a dramatic rise in ionization and temperature within $\sim$14 hr that is temporally consistent with the blueward evolution of the $w2-v$ color (e.g., Figure 1). There may also be a detection of O IV λ3410 but the lower signal-to-noise ratio in that spectral region makes the line identification uncertain. Interestingly, the detection of O IV/V has only been confirmed in one other SN II, SN 2013fs, and in that object the timescale of this emission was <0.5 days (Yaron et al. 2017). Notably, the shift in ionization seen in SN 2024ggi was also observed in SN 2023ixf but at later phases of +1.1–2.4 days (Jacobson-Galán et al. 2023). A two-component Lorentzian model fit to the Hα profile to the +1.5 day Kast spectrum shows a narrow component FWHM velocity of <270 km s^{-1} that traces the unshocked CSM combined with a broad symmetric component with a velocity of $\sim$1320 km s^{-1} that is caused by the scattering of recombination line photons by free, thermal electrons in the ionized CSM (Chugai 2001; Dessart et al. 2009; Huang & Chevalier 2018). However, the narrow

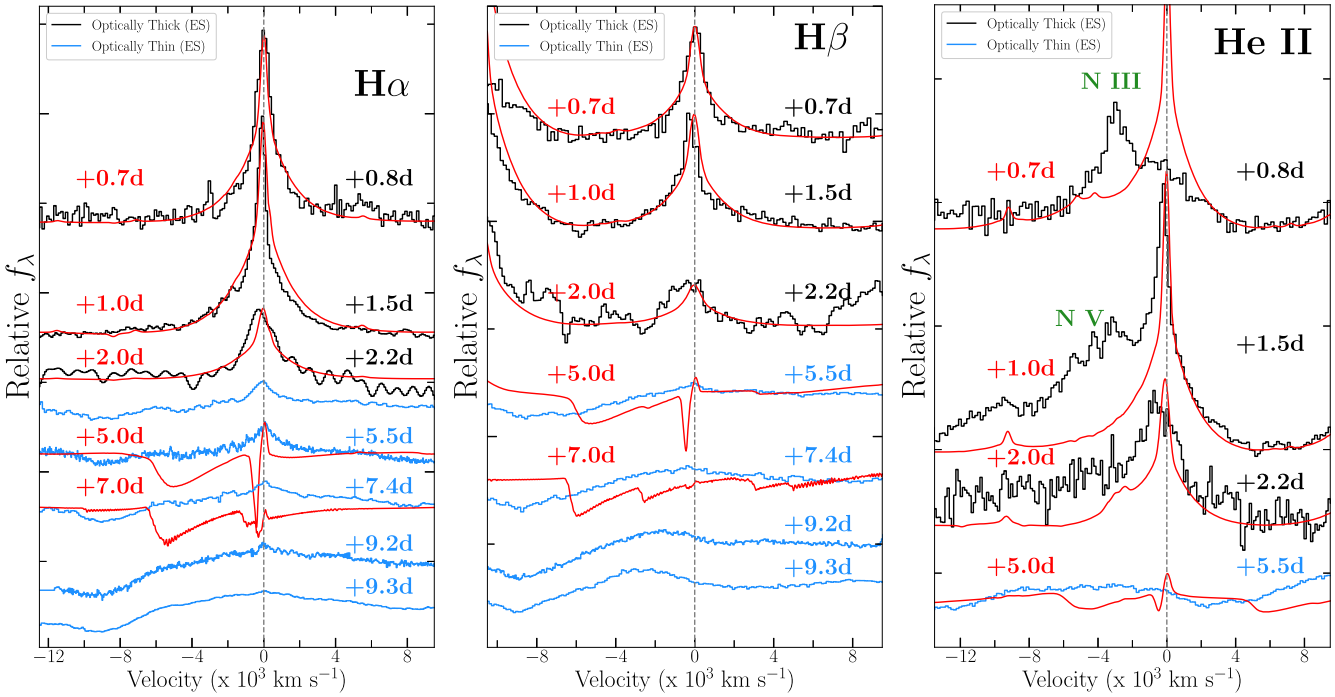

Figure 5. Left: Hα velocity evolution of SN 2024ggi (black) from $\delta t = 0.8$–9.3 days with respect to the r1w6 model spectra (red), which have been scaled to the emission line peaks of SN 2024ggi and smoothed with a Gaussian filter to better compare with the data. Early-time spectral profiles are shaped by electron scattering in the dense CSM. The transition shown from black to blue lines ($t_{\rm IIn} = 3.7 \pm 1.8$ days) marks the emergence of broad absorption features derived from the fastest-moving SN ejecta. Middle: Hβ velocity evolution, also showing that the electron-scattering line profiles subside by ∼5.5 days. Right: He II λ4686 velocity evolution reveals that the electron-scattering profile fades by ∼5.5 days, suggesting a significant decrease in CSM density.

component is likely affected by radiative acceleration of the CSM, which causes the width of the narrow component to be larger than the true velocity of the progenitor wind (Dessart et al. 2015, 2017; Tsuna et al. 2023).

In addition to optical spectroscopy, we present NIR spectra of SN 2024ggi in Figure 3 that extend from 0.9 to 2.4 μm. The first spectrum at $\delta t = 2.2$ days shows IIn-like features of He II as well as hydrogen Paschen and Brackett transitions of Pδ, Pγ, Pβ, and Bγ. We then compare this spectrum to SN II SN 2017ahn (Tartaglia et al. 2021), one of the only SNe with IIn-like features to have an NIR spectrum during the dense CSM-interaction phase. Overall, the NIR spectrum of SN 2024ggi at $\delta t = 2.2$ days shows similar narrow emission lines to SN 2017ahn with the exception being that SN 2017ahn shows prominent He I emission while SN 2024ggi only shows He II.

As shown in Figure 5, the IIn-like features in SN 2024ggi are already fading by the +2.2 day epoch, with possible blueshifted, Doppler-broadened He II emission as the fastest-moving ejecta and/or the dense shell starts to become visible given a decrease in optical depth. Then, by $\delta t = 5.5$ days, the IIn-like features have vanished and SN 2024ggi shows a broad, blueshifted absorption profile in all Balmer transitions as well as a blueshifted He II profile extending out to $\sim(10–12) \times 10^4$ km s^{-1} (i.e., a "ledge feature;" Dessart et al. 2016; Hosseinzadeh et al. 2022; Chugai & Utrobin 2023; Pearson et al. 2023; Shrestha et al. 2024). Based on this evolution, we estimate the duration of the IIn-like line profiles to be $t_{\rm IIn} = 3.8 \pm 1.6$ days, which marks the transition point at which the optical depth to electron scattering has dropped enough to see the emerging fast-moving SN ejecta. At $\delta t > 5$ days, we observe broad absorption profiles in the Hα and Hβ transitions that extend to ∼12,000 km s^{-1}, which provides a decent estimate of the velocities of the fastest-moving H-rich material at the shock front. Using the estimated $t_{\rm IIn}$ and a shock velocity of $v_{\rm sh} = 12{,}000$ km s^{-1}, the transition to lower-density CSM likely occurs at a radius of $r = R_\star + v_{\rm sh} \times t_{\rm IIn} = (4.3 \pm 1.7) \times 10^{14}$ cm (for $R_\star = 500\ R_\odot$) and at a CSM density of $\rho = (\kappa_{\rm T} \times t_{\rm IIn} \times v_{\rm sh})^{-1} = (7.4 \pm 3.1) \times 10^{-15}$ g cm^{-3}, for $\tau = 1$ and a Thompson opacity of $\kappa_{\rm T} = 0.34$ cm^2 g^{-1}. This likely indicates a more confined CSM and/or lower mass-loss rate for SN 2024ggi than the Class 1 gold- and silver-sample SNe II that have $t_{\rm IIn} > 5$ days, e.g., SNe 2017ahn, 2018zd, 2020pni, 2020tlf, and 2023ixf. However, as shown in Figure 4, the duration of IIn-like features in SN 2024ggi is similar to the Class 2 and 3 objects, which reveals that if earlier time spectra (e.g., $\delta t < 1$ day) had been obtained for these objects, they may have shown N III emission like the Class 1 objects and SN 2024ggi at $\delta t < 1$ day.

3.3. Model Matching

In order to quantify the CSM properties of SN 2024ggi, we compared the spectral and photometric properties of SN 2024ggi to a model grid of radiation hydrodynamics and NLTE radiative-transfer simulations covering a wide range of progenitor mass-loss rates ($\dot{M} = 10^{-6}$–$10^{0}\ M_\odot$ yr^{-1} and $v_w = 50$ km s^{-1}) and CSM radii ($R = 10^{14}$–10^{16} cm), all in spherical symmetry. Density profiles for a representative set of models are present in Figure 6. Simulations of the SN ejecta–CSM interaction were performed with the multigroup radiation-hydrodynamics code HERACLES (González et al. 2007; Vaytet et al. 2011; Dessart et al. 2015), which consistently computes the radiation field and hydrodynamics. Then, at selected snapshots in time postexplosion, the hydrodynamical variables are imported into the NLTE radiative-transfer code CMFGEN (Hillier & Dessart 2012; Dessart et al. 2015) for an accurate

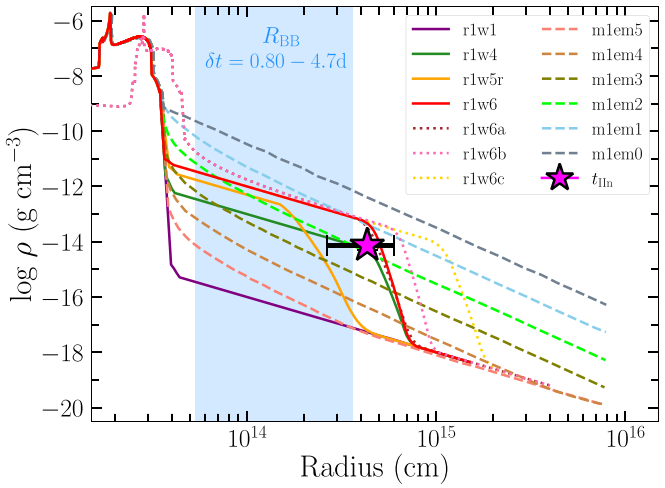

Figure 6. CSM densities and radii for a subset of the CMFGEN model grid used in Jacobson-Galán et al. (2024). Best-matched models to SN 2024ggi (Section 3.3) are r1w6 (solid red line), m1em2 (dashed lime-green line), r1w4 (solid dark green line), and r1w5r (solid orange line). Blackbody radii between $\delta t = 0.8$–4.7 days are shown in the light blue shaded region. The transition point where the CSM goes from optically thick to thin to electron scattering is shown as a magenta star (Section 3.2).

calculation of the radiative transfer, which includes a complete model atom, $\sim 10^6$ frequency points, and treatment of continuum and line processes as well as noncoherent electron scattering. For each model, we adopt an explosion energy of 1.2×10^{51} erg, a 15 $M_\odot$ progenitor with a radius ranging from $R_\star \approx 500$–700 $R_\odot$, and a CSM composition set to the surface mixture of an RSG progenitor (Dessart et al. 2017). For the simulations presented in this work, the CSM extent is much greater than $R_\star$ ($\sim$500–1200 $R_\odot$ for an RSG mass range of $\sim$10–20 $M_\odot$) and $R_\star$ has little impact during phases of ejecta–CSM interaction. The progenitor radius plays a more significant role on the light-curve evolution during the plateau phase (e.g., see Dessart et al. 2013; Jacobson-Galán et al. 2022), i.e., once the interaction phase is over and the emission from the deeper ejecta layers dominates the SN luminosity. Specific methods for each simulation can be found in Dessart et al. (2016, 2017), Jacobson-Galán et al. (2022), and Dessart & Jacobson-Galán (2023).

We determine the best-matched model to SN 2024ggi through direct spectral matching and the peak and rise time in all available UV–optical filters (see Jacobson-Galán et al. 2024 for specifics of the model-matching procedure). As shown in Figure 2, the early-time evolution of SN 2024ggi is most consistent with the r1w6 model, suggesting a mass-loss rate of $\dot{M} = 10^{-2}$ $M_\odot$ yr^{-1} and a dense CSM (i.e., optically thick to electron scattering) that extends to $\sim 5 \times 10^{14}$ cm. In Figure 5 we show that the line profiles in SN 2024ggi during the first few days of SN 2024ggi are decently matched by the r1w6 model and that a lower mass-loss rate model (e.g., $\dot{M} = 5 \times 10^{-3}$ $M_\odot$ yr^{-1}, r1w5r) cannot match the duration of the IIn-like features. However, notable differences include the lack of N III and the strong He II at +0.8 days that are not present in SN 2024ggi and the inability of the r1w6 model to adequately reproduce the complete N III/He II complex, i.e., the model profile is too narrow as was observed in SN 2023ixf (Jacobson-Galán et al. 2023), which could be due to the fact that these simulations assume spherical symmetry and/or require higher kinetic energies. After t_{IIn}, the r1w6 model spectra show a narrow P Cygni profile combined with broad absorption that extends to $\sim$7000 km s^{-1} in Balmer transitions. However, while this is qualitatively the behavior observed in SN 2024ggi, there is no narrow P Cygni feature observed until the +9.3 day spectra and the absorption profiles in SN 2024ggi extend to much larger velocities of $\sim$12,000 km s^{-1}. This mismatch is likely due to increased ejecta deceleration in the models that is not present in SN 2024ggi and/or the CSM of SN 2024ggi is asymmetric, allowing for some parts of the SN ejecta that only encounter low-density CSM to retain higher velocities. Asymmetric CSM has been proposed for similar events such as SNe 1998S and 2023ixf (Leonard et al. 2000; Vasylyev et al. 2023) based on spectropolarimetry. Similar to SN 2023ixf, CSM asymmetry may need to be invoked if the densities inferred from X-ray detections (Margutti & Grefenstette 2024; Zhang et al. 2024) deviate from those inferred from the early-time UV–optical light curve and spectra. Furthermore, it is expected that the dense shell formed from postshock gas should break up, even for a spherical explosion and spherical CSM, which would lead to a much more complicated structure than is obtained when spherical symmetry is imposed.

In addition to direct spectral comparison, we also use the peak absolute magnitudes and rise times in all UV–optical filters to determine the best-matched models from the CMFGEN grid. Using the residuals between the model predictions and observables, we find that SN 2024ggi is best matched by the r1w4, m1em2, r1w6, and r1w6b models, which have a mass-loss range of $\dot{M} = (0.1$–$1) \times 10^{-2}$ $M_\odot$ yr^{-1} and radii of dense CSM that ranges from $r = 4$–8×10^{14} cm. We note that the m1em2 model (Dessart & Jacobson-Galán 2023) does not have a confined shell of dense CSM but rather has a continuous r^{-3} density profile that extends to 10^{16} cm (e.g., see Figure 6). Furthermore, the r1w4 model ($\dot{M} = 10^{-3}$ $M_\odot$ yr^{-1}) cannot reproduce the spectral evolution of SN 2024ggi because the IIn-like features are not sustained for a long enough timescale. Additionally, matching the observed t_{IIn} in SN 2024ggi to the model grid produces only three consistent models: m1em2, r1w6, and r1w6a, all with $\dot{M} = 10^{-2}$ $M_\odot$ yr^{-1}. As shown in Figure 1, the complete m1em2 and r1w6a model light curves provide a decent match to the multiband SN 2024ggi light curve at maximum light but cannot capture the steep rise to peak. This inconsistency is likely the result of the CSM density profile immediately beyond $R_\star$ and/or the limitations of the simulations at very early phases (e.g., $\delta t < 1$ day), e.g., light travel time effects which are considered in the radiation-hydrodynamics simulations but are not included in the computation of the resulting spectrum.

4. Discussion

Observations of SN 2024ggi for 2 weeks after first light have helped to constrain both the explosion dynamics and physics as well as progenitor activity prior to core collapse. Specifically, the observed change in ionization present in the $\sim$0.8–1.5 day spectra (Figure 5) and the rise in temperature shown by the red-to-blue color evolution (Figure 1) suggest that we caught the SN as the shock broke out of the optically thick envelope and into the extended, dense, and initially cold CSM. Rather than a prompt rise in temperature to $\sim 10^5$ K, the CSM heats up to a lower temperature and becomes progressively more ionized (e.g., He I/II, C III/IV, or N III/IV/V) on a $\sim$1–2 day timescale as the radiative precursor, and then the radiation from the shock/ejecta, diffuses through the CSM. Furthermore, a

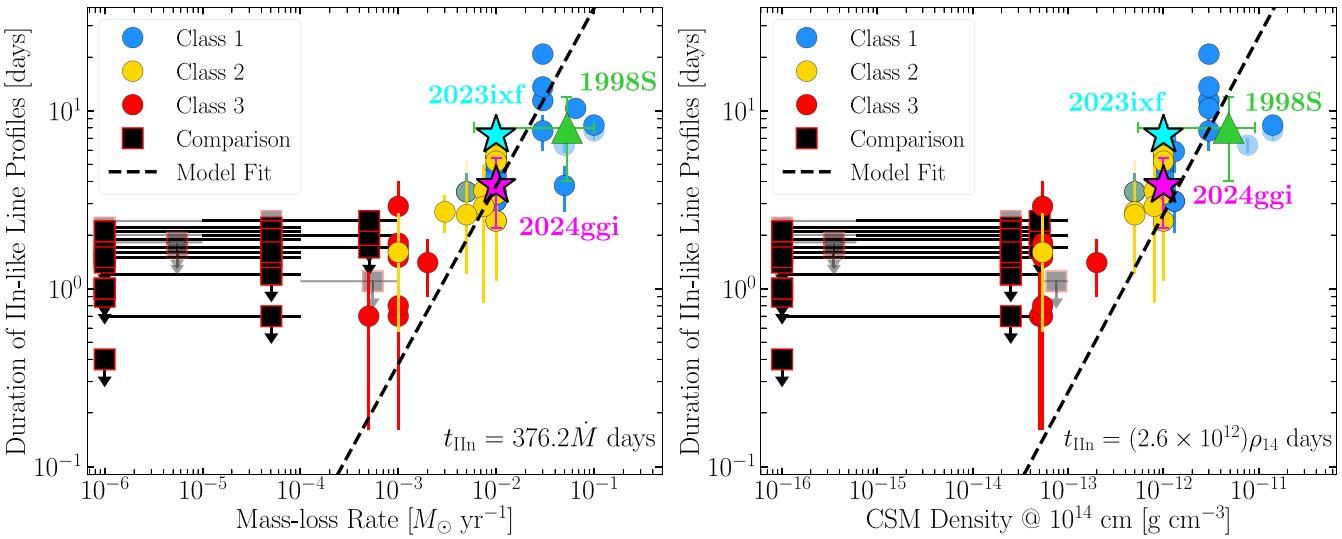

Figure 7. Duration of IIn-like features vs. mass-loss rates (left) and CSM densities at $r = 10^{14}$ cm (right) derived from direct spectral matching for the gold- and silver- (blue, yellow, and red circles) and comparison-sample (black squares) objects presented in Jacobson-Galán et al. (2024). Solid colored points represent the subsample of objects at $D > 40$ Mpc. The best-matched mass-loss rate and CSM density at $r = 10^{14}$ cm for SN 2024ggi obtained from spectral matching (Section 3.3) are shown as a magenta star. SNe 1998S and 2023ixf are shown for reference as a green triangle and cyan star, respectively.

comparison of the spectral series, $t_{\rm IIn}$, peak luminosities, and rise times to a grid of CMFGEN models indicates that the progenitor of SN 2024ggi was likely an RSG with a mass-loss rate of $\dot{M} \approx 10^{-2}\,M_\odot$ yr^{-1}, which created dense CSM extending to $r \approx 5 \times 10^{14}$ cm that contained a total mass of $M_{\rm CSM} \approx 0.02$–$0.04\ M_\odot$. This range of CSM mass is consistent with simulations of RSG mass loss through energy injection within convective RSG envelopes (Tsang et al. 2022), pre-SN outbursts (Takei et al. 2022), and RSG "boil-off" (Fuller & Tsuna 2024). We also find that the observed light curve can be matched with a standard explosion energy (1.2×10^{51} erg) and that the IIn-like signatures in SN 2024ggi can be modeled with a CSM composition that matches typical RSG surface abundances, which suggests that significant N or He enrichment to the CSM may not be required.

For a wind velocity of $\sim$50 km s^{-1}, the proposed CSM extent translates to a period of enhanced mass loss in the last $\sim$3 yr prior to core collapse. Similarly, for the observed $t_{\rm IIn}$ and a shock velocity of $v_{\rm sh} = 12{,}000$ km s^{-1}, the dense CSM would extend to $r \approx (4.3 \pm 1.7) \times 10^{14}$ cm and would indicate enhanced mass loss in the final $\sim$1.4–3.6 yr before first light, for a progenitor wind velocity of 50 km s^{-1}. However, it should be noted that this timescale may not be accurate for enhanced wind scenarios (e.g., Davies et al. 2022) because the timescales for wind acceleration to a terminal velocity can take longer than the above pre-SN timescale. From the spectral evolution of SN 2024ggi in its first 2 weeks, it is clear that a reduction in CSM density did occur at $\sim$3.8 days because as the CSM optical depth to electron scattering drops below unity, the Lorentzian wings of the IIn-like features disappear and absorption profiles from the fastest-moving material become visible. However, the open question is whether the CSM detected in SN 2024ggi represents only the high-density shell of CSM (i.e., only one phase of enhanced mass loss) that extends to $r < 5 \times 10^{14}$ cm (e.g., the r1w6 model density profile) or if SN 2024ggi sustained enhanced mass loss for several decades before explosion (e.g., the m1em2 model density profile). As was done for SN 2023ixf, future multi-wavelength monitoring will be able to determine the CSM density at larger scales as the SN shock samples material that was liberated from the progenitor star years to decades before explosion (Berger et al. 2023; Grefenstette et al. 2023; Panjkov et al. 2023; Chandra et al. 2024; A. J. Nayana et al. 2024, in preparation). Overall, both the confined high-density CSM shell and the extended low-density wind may have made the RSG progenitor star quite dust obscured prior to explosion (Davies et al. 2022), similar to what was revealed by preexplosion imaging of the SN 2023ixf RSG progenitor (Jencson et al. 2023; Kilpatrick et al. 2023; Niu et al. 2023; Qin et al. 2023; Soraisam et al. 2023; Van Dyk et al. 2024).

As shown in Figures 4 and 7, the observables and best-matched CSM properties of SN 2024ggi reside naturally within the continuum of SNe II, both with and without spectroscopic signatures of interaction with dense CSM. SN 2024ggi's best-matched $\dot{M}$ and CSM density at 10^{14} cm is lower than that inferred for more extreme Class 1 events such as SNe 1998S, 2017ahn, 2018zd, 2020tlf, 2020pni, and 2023ixf, all of which likely have higher mass-loss rates, and/or dense CSM that extends to larger radii. Nonetheless, SN 2024ggi's evolution requires a progenitor mass-loss rate that is significantly higher than what is inferred for standard SNe II as well as what is measured in local RSGs (Beasor et al. 2020). Overall, this continues to point toward a phase of enhanced mass loss in the final years before explosion for some significant fraction of RSGs.

5. Conclusions

In this paper, we have presented UV–optical–NIR observations of the nearby SN II, SN 2024ggi located in the nearby spiral host galaxy NGC 3621 at $D = 7.2$ Mpc. Below we summarize the primary observational findings of SN 2024ggi.

1. The first optical spectrum of SN 2024ggi shows prominent narrow emission lines of H I, He I, N III, and C III that result from the photoionization of dense, optically thick CSM. Between $\delta t = 0.8$–1.5 days, SN 2024ggi exhibits a detectable rise in temperature and ionization that manifests as the appearance of higher

ionization species such as He II, N IV/V, C IV, and O V. This spectral evolution is temporally consistent with a dramatic red-to-blue evolution in $w2-v$ color and an increasing blackbody temperature. These phenomena suggest that SN 2024ggi was observed during the initial precursor associated with SBO inside dense CSM.

2. SN 2024ggi displayed electron-scattering-broadened profiles (i.e., IIn-like) that persist on a characteristic timescale of $t_{\rm IIn} = 3.8 \pm 1.6$ days, after which time a decrease in optical depth to electron scattering due to a reduction in CSM density allows for the detection of broad absorption profiles from the fastest H-rich SN ejecta.
3. Interaction of the SN 2024ggi ejecta with dense, confined CSM yielded peak UV–optical absolute magnitudes (e.g., $M_{\rm w2} = -18.7$ mag and $M_{\rm g} = -18.1$ mag, respectively) that are consistent with other SNe II with IIn-like features presented in sample studies (e.g., Jacobson-Galán et al. 2024).
4. Comparison of SN 2024ggi's spectral evolution, peak absolute magnitudes, rise time, and duration of IIn-like profiles to a grid of CMFGEN simulations suggests a CSM that has a composition typical of a solar-metallicity RSG, confined to $r < 5 \times 10^{14}$ cm, and which formed from a progenitor mass-loss rate of $\dot{M} = 10^{-2}\,M_{\odot}$ yr^{-1} (i.e., $\rho \approx 10^{-12}$ g cm^{-3} at $r = 10^{14}$ cm). Adopting a wind velocity of $v_w = 50$ km s^{-1}, this scenario corresponds to a period of enhanced mass loss during the last $\sim$3 yr before core collapse.
5. SN 2024ggi is similar to SN 2023ixf in its rise in ionization within of order days of first light and the high-ionization species present in its early-time spectra; both objects were likely observed during SBO within dense CSM. However, SN 2024ggi has a shorter timescale of IIn-like features ($\sim$4 days versus $\sim$7 days) and a more compact CSM ($<5 \times 10^{14}$ cm versus $(0.5–1) \times 10^{15}$ cm) despite a similar mass-loss rate and CSM density at 10^{14} cm.

Like SN 2023ixf, SN 2024ggi represents a unique opportunity to study the long-term, multiwavelength evolution of an SN II that interacts with dense, confined CSM in exquisite detail. Future studies and multiwavelength observations will probe the nature and late-stage evolution of the progenitor star as well as uncover the properties of the large-scale circumstellar environment, both of which are tracing an unconstrained period of RSG evolution before core collapse.

Acknowledgments

Research at UC Berkeley is conducted on the territory of Huichin, the ancestral and unceded land of the Chochenyo-speaking Ohlone people, the successors of the sovereign Verona Band of Alameda County. The Shane 3 m observations were conducted on the land of the Ohlone (Costanoans), Tamyen, and Muwekma Ohlone tribes.

W.J.-G. is supported by the National Science Foundation Graduate Research Fellowship Program under grant No. DGE-1842165. W.J.-G. acknowledges support through NASA grants in support of Hubble Space Telescope programs GO-16075 and 16500. This research was supported in part by the National Science Foundation under grant No. NSF PHY-1748958. R.M. acknowledges support from the National Science Foundation under Award Nos. AST-2221789 and AST-2224255. The Margutti team at UC Berkeley is partially funded by the Heising-Simons Foundation under grants #2018-0911 and #2021-3248 (PI: Margutti).

M.R.D. acknowledges support from the NSERC through grant RGPIN-2019-06186, the Canada Research Chairs Program, and the Dunlap Institute at the University of Toronto. Parts of this research were supported by the Australian Research Council Discovery Early Career Researcher Award (DECRA) through project number DE230101069. Y.-C.P. is supported by the National Science and Technology Council (NSTC grant 109-2112-M-008-031-MY3). C.G. is supported by a VILLUM FONDEN Young Investigator Grant (project number 25501). D. M. acknowledges NSF support from grants PHY-2209451 and AST-2206532. A.S. acknowledges the financial support from CNPq (402577/2022-1). G.D. is supported by the H2020 European Research Council grant No. 758638. C.R.B. acknowledges the financial support from CNPq (316072/2021-4), from FAPERJ (grants 201.456/2022 and 210.330/2022), and the FINEP contract 01.22.0505.00 (ref. 1891/22). This research is based on observations made with the Thai Robotic Telescope under program ID TRTC11B006, which is operated by the National Astronomical Research Institute of Thailand (Public Organization). Part of the data were obtained with the REM telescope, located in Chile and operated by the d'REM team for INAF. This work is supported by the National Science Foundation under Cooperative Agreement PHY-2019786 (The NSF AI Institute for Artificial Intelligence and Fundamental Interactions; http://iaifi.org/).

The UCSC team is supported in part by NASA grants NNG17PX03C and 80NSSC22K1518, NSF grant AST-1815935, and by a fellowship from the David and Lucile Packard Foundation to R.J.F.

YSE-PZ (Coulter et al. 2023) was developed by the UC Santa Cruz Transients Team with support from NASA grants NNG17PX03C, 80NSSC19K1386, and 80NSSC20K0953; NSF grants AST-1518052, AST-1815935, and AST-1911206; the Gordon & Betty Moore Foundation; the Heising-Simons Foundation; a fellowship from the David and Lucile Packard Foundation to R.J.F.; Gordon and Betty Moore Foundation postdoctoral fellowships and a NASA Einstein fellowship, as administered through the NASA Hubble Fellowship program and grant HST-HF2-51462.001 to D.O. J.; and a National Science Foundation Graduate Research Fellowship, administered through grant No. DGE-1339067 to D.A.C.

A major upgrade of the Kast spectrograph on the Shane 3 m telescope at Lick Observatory, led by Brad Holden, was made possible through generous gifts from the Heising-Simons Foundation, William and Marina Kast, and the University of California Observatories. Research at Lick Observatory is partially supported by a generous gift from Google.

This work has made use of data from the Asteroid Terrestrial-impact Last Alert System (ATLAS) project. The Asteroid Terrestrial-impact Last Alert System (ATLAS) project is primarily funded to search for near-Earth asteroids through NASA grants NN12AR55G, 80NSSC18K0284, and 80NSSC18K1575; by-products of the NEO search include images and catalogs from the survey area. This work was partially funded by Kepler/K2 grant J1944/80NSSC19K0112 and HST GO-15889, and STFC grants ST/T000198/1 and ST/S006109/1. The ATLAS science products have been made

possible through the contributions of the University of Hawaii Institute for Astronomy, the Queen's University Belfast, the Space Telescope Science Institute, the South African Astronomical Observatory, and The Millennium Institute of Astrophysics (MAS), Chile.

This research was supported by the Munich Institute for Astro-, Particle and BioPhysics (MIAPbP), which is funded by the Deutsche Forschungsgemeinschaft (DFG, German Research Foundation) under Germany's Excellence Strategy —EXC-2094—390783311.

IRAF is distributed by NOAO, which is operated by AURA, Inc., under cooperative agreement with the National Science Foundation (NSF).

Facilities: ATLAS, Gemini:South (GMOS), SOAR (Goodman/TSpec), Shane (Kast), LCOGT, LO:1m, CTIO:1.0m.

Software: IRAF, photpipe (Rest et al. 2005), DoPhot (Schechter et al. 1993), HOTPANTS (Becker 2015), YSE-PZ (Coulter et al. 2022, 2023), `CMFGEN` (Hillier & Dessart 2012; Dessart et al. 2015), `HERACLES` (González et al. 2007; Vaytet et al. 2011; Dessart et al. 2015), HEAsoft (v6.33), and DRAGONS (Labrie et al. 2023).

Appendix

Here we present a log of optical spectroscopic observations of SN 2024ggi in Table A1.

Table A1
Optical Spectroscopy of SN 2024ggi

UT Date	MJD	Phase[a] (days)	Telescope	Instrument	Wavelength Range (Å)
2024-04-12T06:10:08.92	60412.26	1.46	Shane	Kast	3254–10495
2024-04-13T00:00:05.88	60413.00	2.20	SOAR	TripleSpec	8243.4–24667.1
2024-04-13T00:41:21.57	60413.03	2.22	SOAR	Goodman	3816–7030
2024-04-16 06:21:35.01	60416.26	5.46	Shane	Kast	3603–10293
2024-04-16T06:34:06.69	60416.27	5.47	Shane	Kast	5800–7000
2024-04-18T05:49:43.62	60418.24	7.44	Shane	Kast	3253–10494
2024-04-19T23:41:17.00	60419.99	9.19	Gemini-S	GMOS	4000–7580
2024-04-20T01:32:39.64	60420.06	9.26	SOAR	TripleSpec	8243.0–24667.5
2024-04-20T02:19:26.89	60420.10	9.30	SOAR	Goodman	3854–8986

Note.
[a] Relative to first light (MJD 60410.80).

ORCID iDs

W. V. Jacobson-Galán https://orcid.org/0000-0002-3934-2644
K. W. Davis https://orcid.org/0000-0002-5680-4660
C. D. Kilpatrick https://orcid.org/0000-0002-5740-7747
L. Dessart https://orcid.org/0000-0003-0599-8407
R. Margutti https://orcid.org/0000-0003-4768-7586
R. Chornock https://orcid.org/0000-0002-7706-5668
R. J. Foley https://orcid.org/0000-0002-2445-5275
P. Arunachalam https://orcid.org/0000-0002-6688-3307
K. Auchettl https://orcid.org/0000-0002-4449-9152
C. R. Bom https://orcid.org/0000-0003-4383-2969
R. Cartier https://orcid.org/0000-0003-4553-4033
D. A. Coulter https://orcid.org/0000-0003-4263-2228
G. Dimitriadis https://orcid.org/0000-0001-9494-179X
D. Dickinson https://orcid.org/0000-0003-0913-4120
M. R. Drout https://orcid.org/0000-0001-7081-0082
A. T. Gagliano https://orcid.org/0000-0003-4906-8447
C. Gall https://orcid.org/0000-0002-8526-3963
B. Garretson https://orcid.org/0000-0001-6922-8319
L. Izzo https://orcid.org/0000-0001-9695-8472
D. O. Jones https://orcid.org/0000-0002-6230-0151
N. LeBaron https://orcid.org/0000-0002-2249-0595
H.-Y. Miao https://orcid.org/0000-0003-2736-5977
D. Milisavljevic https://orcid.org/0000-0002-0763-3885
Y.-C. Pan https://orcid.org/0000-0001-8415-6720
A. Rest https://orcid.org/0000-0002-4410-5387
C. Rojas-Bravo https://orcid.org/0000-0002-7559-315X
A. Santos https://orcid.org/0000-0002-1420-3584
H. Sears https://orcid.org/0000-0001-8023-4912
B. M. Subrayan https://orcid.org/0000-0001-8073-8731
K. Taggart https://orcid.org/0000-0002-5748-4558
S. Tinyanont https://orcid.org/0000-0002-1481-4676

References

Andrews, J. E., Pearson, J., Hosseinzadeh, G., et al. 2024, ApJ, 965, 85
Antonelli, L. A., Zerbi, F. M., Chincarini, G., et al. 2003, MmSAI, 74, 304
Beasor, E. R., Davies, B., Smith, N., et al. 2020, MNRAS, 492, 5994
Becker, A. 2015, HOTPANTS: High Order Transform of PSF ANd Template Subtraction, Astrophysics Source Code Library, ascl:1504.004
Berger, E., Keating, G., Alexander, K., et al. 2023, TNSAN, 131, 1
Bostroem, K. A., Pearson, J., Shrestha, M., et al. 2023, ApJL, 956, 17
Brown, P. J., Breeveld, A. A., Holland, S., Kuin, P., & Pritchard, T. 2014, Ap&SS, 354, 89
Bruch, R. J., Gal-Yam, A., Schulze, S., et al. 2021, ApJ, 912, 46
Bruch, R. J., Gal-Yam, A., Yaron, O., et al. 2023, ApJ, 952, 119
Chandra, P., Chevalier, R. A., Maeda, K., Ray, A. K., & Nayana, A. J. 2024, ApJL, 963, L4
Chen, T.-W., Yang, S., Srivastav, S., et al. 2024, arXiv:2406.09270
Chevalier, R. A., & Fransson, C. 2017, in Handbook of Supernovae, ed. A. W. Alsabti & P. Murdin (Berlin: Springer), 875
Chevalier, R. A., & Irwin, C. M. 2011, ApJL, 729, L6
Chevalier, R. A., & Irwin, C. M. 2012, ApJL, 747, L17
Chugai, N. N. 2001, MNRAS, 326, 1448
Chugai, N. N., & Utrobin, V. P. 2023, AstL, 49, 639
Clemens, J. C., Crain, J. A., & Anderson, R. 2004, Proc. SPIE, 5492, 331
Coulter, D. A., Jones, D. O., McGill, P., et al. 2022, YSE-PZ: An Open-source Target and Observation Management System, v0.3.0, Zenodo, doi:10.5281/zenodo.7278430
Coulter, D. A., Jones, D. O., McGill, P., et al. 2023, PASP, 135, 064501
Cushing, M. C., Vacca, W. D., & Rayner, J. T. 2004, PASP, 116, 362
Dastidar, R., Pignata, G., Dukiya, N., et al. 2024, A&A, 685, A44
Davies, B., Plez, B., & Petrault, M. 2022, MNRAS, 517, 1483
Dessart, L., Audit, E., & Hillier, D. J. 2015, MNRAS, 449, 4304
Dessart, L., Hillier, D. J., Audit, E., Livne, E., & Waldman, R. 2016, MNRAS, 458, 2094
Dessart, L., Hillier, D. J., Gezari, S., Basa, S., & Matheson, T. 2009, MNRAS, 394, 21
Dessart, L., Hillier, D. J., Waldman, R., & Livne, E. 2013, MNRAS, 433, 1745
Dessart, L., & Jacobson-Galán, W. V. 2023, A&A, 677, A105
Dessart, L., John Hillier, D., & Audit, E. 2017, A&A, 605, A83
Finkbeiner, D. P., Schlafly, E. F., Schlegel, D. J., et al. 2016, ApJ, 822, 66
Fitzpatrick, E. L. 1999, PASP, 111, 63
Fuller, J., & Tsuna, D. 2024, OJAp, 7, 47
Gal-Yam, A., Arcavi, I., Ofek, E. O., et al. 2014, Natur, 509, 471
Gehrels, N., Chincarini, G., Giommi, P., et al. 2004, ApJ, 611, 1005
Goldberg, J. A., Jiang, Y.-F., & Bildsten, L. 2022, ApJ, 933, 164
González, M., Audit, E., & Huynh, P. 2007, A&A, 464, 429
Grefenstette, B. W., Brightman, M., Earnshaw, H. P., Harrison, F. A., & Margutti, R. 2023, ApJL, 952, L3
Haynie, A., & Piro, A. L. 2021, ApJ, 910, 128
Hillier, D. J., & Dessart, L. 2012, MNRAS, 424, 252
Hiramatsu, D., Howell, D. A., Van Dyk, S. D., et al. 2021, NatAs, 5, 903
Hiramatsu, D., Tsuna, D., Berger, E., et al. 2023, ApJL, 955, L8
Hoogendam, W., Auchettl, K., Tucker, M., et al. 2024, TNSAN, 103, 1
Horne, K. 1986, PASP, 98, 609
Hosseinzadeh, G., Valenti, S., McCully, C., et al. 2018, ApJ, 861, 63
Hosseinzadeh, G., Kilpatrick, C. D., Dong, Y., et al. 2022, ApJ, 935, 31
Hosseinzadeh, G., Farah, J., Shrestha, M., et al. 2023, ApJL, 953, L16
Huang, C., & Chevalier, R. A. 2018, MNRAS, 475, 1261
Irani, I., Morag, J., Gal-Yam, A., et al. 2024, ApJ, 970, 96
Jacobson-Galán, W. V., Dessart, L., Jones, D. O., et al. 2022, ApJ, 924, 15
Jacobson-Galán, W. V., Dessart, L., Margutti, R., et al. 2023, ApJL, 954, L42
Jacobson-Galán, W. V., Dessart, L., Davis, K. W., et al. 2024, ApJ, 970, 189
Jencson, J. E., Pearson, J., Beasor, E. R., et al. 2023, ApJL, 952, L30
Khazov, D., Yaron, O., Gal-Yam, A., et al. 2016, ApJ, 818, 3
Kilpatrick, C. D., Takaro, T., Foley, R. J., et al. 2018, MNRAS, 480, 2072
Kilpatrick, C. D., Foley, R. J., Jacobson-Galán, W. V., et al. 2023, ApJL, 952, L23
Kirkpatrick, J. D., Cushing, M. C., Gelino, C. R., et al. 2011, ApJS, 197, 19
Labrie, K., Simpson, C., Cardenes, R., et al. 2023, RNAAS, 7, 214
Leonard, D. C., Filippenko, A. V., Barth, A. J., & Matheson, T. 2000, ApJ, 536, 239
Li, G., Hu, M., Li, W., et al. 2024, Natur, 627, 754
Margutti, R., & Grefenstette, B. 2024, ATel, 16587, 1
McCully, C., Volgenau, N. H., Harbeck, D.-R., et al. 2018, Proc. SPIE, 10707, 107070K
Miller, J. S., & Stone, R. P. S. 1993, Lick Observatory Technical Reports 66, Univ. California
Moriya, T. J., Subrayan, B. M., Milisavljevic, D., & Blinnikov, S. I. 2023, PASJ, 75, 634
Nakaoka, T., Kawabata, K. S., Maeda, K., et al. 2018, ApJ, 859, 78
NASA High Energy Astrophysics Science Archive Research Center (Heasarc) 2014, HEAsoft: Unified Release of FTOOLS and XANADU, Astrophysics Source Code Library, ascl:1408.004
Niu, Z., Sun, N.-C., Maund, J. R., et al. 2023, ApJL, 955, L15
Onken, C. A., Wolf, C., Bessell, M. S., et al. 2024, arXiv:2402.02015
Panjkov, S., Auchettl, K., Shappee, B. J., et al. 2023, arXiv:2308.13101
Pearson, J., Hosseinzadeh, G., Sand, D. J., et al. 2023, ApJ, 945, 107
Qin, Y.-J., Zhang, K., Bloom, J., et al. 2023, arXiv:2309.10022
Rest, A., Stubbs, C., Becker, A. C., et al. 2005, ApJ, 634, 1103
Roming, P. W. A., Kennedy, T. E., Mason, K. O., et al. 2005, SSRv, 120, 95
Saha, A., Thim, F., Tammann, G. A., Reindl, B., & Sandage, A. 2006, ApJS, 165, 108
Santos, A., Kilpatrick, C. D., Bom, C. R., et al. 2024, MNRAS, 529, 59
Sarin, N., Hübner, M., Omand, C. M. B., et al. 2024, MNRAS, 531, 1203
Schechter, P. L., Mateo, M., & Saha, A. 1993, PASP, 105, 1342
Schlafly, E. F., & Finkbeiner, D. P. 2011, ApJ, 737, 103
Schlegel, D. J., Finkbeiner, D. P., & Davis, M. 1998, ApJ, 500, 525
Shingles, L., Smith, K. W., Young, D. R., et al. 2021, TNSAN, 7, 1
Shrestha, M., Pearson, J., Wyatt, S., et al. 2024, ApJ, 961, 247
Smith, K. W., Smartt, S. J., Young, D. R., et al. 2020, PASP, 132, 085002
Smith, N., Mauerhan, J. C., Cenko, S. B., et al. 2015, MNRAS, 449, 1876
Smith, N., Pearson, J., Sand, D. J., et al. 2023, ApJ, 956, 46
Soraisam, M. D., Szalai, T., Van Dyk, S. D., et al. 2023, ApJ, 957, 64
Srivastav, S., Chen, T. W., Smartt, S. J., et al. 2024, TNSAN, 100, 1
Stritzinger, M. D., Taddia, F., Burns, C. R., et al. 2018, A&A, 609, A135
Subrayan, B. M., Milisavljevic, D., Moriya, T. J., et al. 2023, ApJ, 945, 46
Takei, Y., Tsuna, D., Kuriyama, N., Ko, T., & Shigeyama, T. 2022, ApJ, 929, 177
Tartaglia, L., Sand, D. J., Groh, J. H., et al. 2021, ApJ, 907, 52
Teja, R. S., Singh, A., Basu, J., et al. 2023, ApJL, 954, L12

Terreran, G., Jacobson-Galán, W. V., Groh, J. H., et al. 2022, ApJ, 926, 20
Terreran, G., Jerkstrand, A., Benetti, S., et al. 2016, MNRAS, 462, 137
Tonry, J., Denneau, L., Weiland, H., et al. 2024, TNSTR, 2024-1020, 1
Tonry, J. L., Denneau, L., Heinze, A. N., et al. 2018, PASP, 130, 064505
Tsang, B. T. H., Kasen, D., & Bildsten, L. 2022, ApJ, 936, 28
Tsuna, D., Murase, K., & Moriya, T. J. 2023, ApJ, 953, 115
Vacca, W. D., Cushing, M. C., & Rayner, J. T. 2003, PASP, 115, 389
Van Dyk, S. D., Srinivasan, S., Andrews, J. E., et al. 2024, ApJ, 968, 27
Vasylyev, S. S., Yang, Y., Filippenko, A. V., et al. 2023, ApJL, 955, L37
Vaytet, N. M. H., Audit, E., Dubroca, B., & Delahaye, F. 2011, JQSRT, 112, 1323
Waxman, E., & Katz, B. 2017, in Handbook of Supernovae, ed. A. W. Alsabti & P. Murdin (Berlin: Springer), 967
Yaron, O., Perley, D. A., Gal-Yam, A., et al. 2017, NatPh, 13, 510
Zhai, Q., Li, L., Zhang, J., & Wang, X. 2024, TNSCR, 2024-1031, 1
Zhang, J., Wang, X., József, V., et al. 2020, MNRAS, 498, 84
Zhang, J., Li, C. K., Cheng, H. Q., et al. 2024, ATel, 16588, 1
Zimmerman, E. A., Irani, I., Chen, P., et al. 2024, Natur, 627, 759